



Nonsaturating large magnetoresistance in semimetals

Ian A. Leahy^a, Yu-Ping Lin^a, Peter E. Siegfried^a, Andrew C. Treglia^a, Justin C. W. Song^b, Rahul M. Nandkishore^{a,c}, and Minhyea Lee^{a,d,1}

^aDepartment of Physics, University of Colorado, Boulder, CO 80309; ^bDivision of Physics and Applied Physics, Nanyang Technological University, Singapore 637371; ^cCenter for Theory of Quantum Matter, University of Colorado, Boulder, CO 80309; and ^dCenter for Experiments on Quantum Materials, University of Colorado, Boulder, CO 80309

Edited by N. Phuan Ong, Princeton University, Princeton, NJ, and approved September 4, 2018 (received for review May 22, 2018)

The rapidly expanding class of quantum materials known as topological semimetals (TSMs) displays unique transport properties, including a striking dependence of resistivity on applied magnetic field, that are of great interest for both scientific and technological reasons. So far, many possible sources of extraordinarily large nonsaturating magnetoresistance have been proposed. However, experimental signatures that can identify or discern the dominant mechanism and connect to available theories are scarce. Here we present the magnetic susceptibility (χ), the tangent of the Hall angle ($\tan \theta_H$), along with magnetoresistance in four different nonmagnetic semimetals with high mobilities, NbP, TaP, NbSb₂, and TaSb₂, all of which exhibit nonsaturating large magnetoresistance (MR). We find that the distinctly different temperature dependences, $\chi(T)$, and the values of $\tan \theta_H$ in phosphides and antimonates serve as empirical criteria to sort the MR from different origins: NbP and TaP are uncompensated semimetals with linear dispersion, in which the nonsaturating magnetoresistance arises due to guiding center motion, while NbSb₂ and TaSb₂ are compensated semimetals, with a magnetoresistance emerging from nearly perfect charge compensation of two quadratic bands. Our results illustrate how a combination of magnetotransport and susceptibility measurements may be used to categorize the increasingly ubiquitous nonsaturating large magnetoresistance in TSMs.

nonsaturating magnetoresistance | magnetic susceptibility | Weyl semimetals | topological semimetals

Magnetoresistance (MR) and the Hall effect are versatile experimental probes in exploring electronic properties of materials, such as carrier density, mobility, and the nature of scattering and disorder. In typical nonmagnetic and semiconducting materials, the MR increases quadratically with applied transverse magnetic field and saturates to a constant value when the product of the applied field and the mobility (ν) approaches unity. Nonsaturating MR is commonly attributed to the semiclassical two-band model, where electron-like and hole-like carriers are nearly compensated (1), resulting in rich magnetotransport characteristics that are strongly temperature (T) and applied transverse magnetic field (H) dependent in nonmagnetic compounds. A flurry of interest in nonsaturating, H -linear MR (2–5) in narrow-gap semiconductors led to two main theoretical accounts: (i) a 2D simple four-terminal resistor network model, where strong disorder or inhomogeneity of the sample manifests as charge and mobility fluctuations (6, 7), and (ii) the so-called “quantum linear MR” which emerges in systems with linear band crossings when the lowest Landau level is occupied (8). The former approach has provided a basis to engineer large magnetotransport responses via macroscopic inhomogeneities or disorder (9–11). Meanwhile, the latter has remained rather elusive until recently.

Interest in nonsaturating very large MR has exploded following the discovery of topological semimetals. These materials are regularly reported to exhibit record-high nonsaturating MR, known as extreme magnetoresistance (XMR), with unusually high mobilities for bulk systems (12–18) and relatively low residual resistivity ρ_0 . The proximity of the chemical potential to

the charge neutrality point in semimetals allows the generic quadratic two-band model to describe the MR and the Hall effect in reasonable levels (19–23). However, a two-band model of this form generically predicts a MR that is quadratic in applied fields, whereas the materials frequently exhibit a MR linear in the applied field. While various theoretical proposals for H linear MR have been advanced (e.g., refs. 8, 24–26), the origins of extreme MR in topological semimetals remain unclear. As nonsaturating, large MR becomes more ubiquitous, it becomes particularly urgent to identify a set of distinct attributes that enable the delineation of their origins.

In this article, we systematically examine the low-field diamagnetic susceptibility (χ), the transverse MR, and the Hall effect as a function of T and H in four different semimetals with high mobility ($\nu \geq 10^4$ cm²/Vs) and very large nonsaturating MR—NbP, TaP (phosphides), NbSb₂, and TaSb₂ (antimonates). Characteristic parameters related to magnetic transport are summarized in Table 1.

We present two different types of nonsaturating large MR identified by the temperature (T) dependence of diamagnetic susceptibility, $\chi(T)$, and the H dependence of the Hall angle, $\tan \theta_H = \frac{\rho_{xy}}{\rho_{xx}} = \frac{\sigma_{xy}}{\sigma_{xx}}$, where ρ_{xx} and ρ_{xy} are longitudinal and Hall resistivity, respectively, and σ_{xx} and σ_{xy} are corresponding conductivities.

One type of MR originates from the presence of smooth disorder that governs guiding center motion of charge carriers. The linear H dependence of this type arises from the squeezed

Significance

The intensive recent investigations of topological semimetals have revealed a large number of semimetal compounds that exhibit very large nonsaturating magnetoresistance. Multiple mechanisms for this magnetoresistance phenomenon have been theoretically proposed, but experimentally it is unclear how to identify which mechanism is responsible in a particular sample or how to make a clean connection between experimental observations and theoretical models. Our results show that the magnetic susceptibility and the tangent of the Hall angle successfully capture the fundamental differences in seemingly similar nonsaturating large magnetoresistance, where charge compensation, energy dispersion, and the roles of disorder are markedly distinct, and provide empirical templates to characterize the origins of the extraordinary magnetotransport properties in the newly discovered topological semimetals and beyond.

Author contributions: M.L. designed research; I.A.L., Y.-P.L., P.E.S., A.C.T., R.M.N., and M.L. performed research; I.A.L., Y.-P.L., J.C.W.S., R.M.N., and M.L. analyzed data; and I.A.L., Y.-P.L., J.C.W.S., R.M.N., and M.L. wrote the paper.

The authors declare no conflict of interest.

This article is a PNAS Direct Submission.

Published under the PNAS license.

¹To whom correspondence should be addressed. Email: minhyea.lee@colorado.edu.

This article contains supporting information online at www.pnas.org/lookup/suppl/doi:10.1073/pnas.1808747115/-DCSupplemental.

Published online October 3, 2018.

Table 1. Summary of magnetotransport data

Sample	$\tan^2\theta_H$	ν, T^{-1}	$\rho_0, \mu\Omega \text{ cm}$	$\Delta\rho/\rho_0$
NbP	7.6	99	0.5	561
TaP	5.8	3.5×10^3	0.2	20,200
NbSb ₂	$\leq 10^{-4}$	1.9–2.5	0.1	27,800
TaSb ₂	$\leq 10^{-4}$	2.2–4.3	0.1	5,560

Residual resistivity ρ_0 at zero field is reported at $T = 2 \text{ K}$ and $\Delta\rho/\rho_0 = (\rho(H) - \rho_0)/\rho_0$ and $\tan^2\theta_H$ at 0.3 K and $\mu_0 H = 15 \text{ T}$.

trajectories of carriers in semiclassically large magnetic fields $\nu B \geq 1$ (easily achieved in linearly dispersing topological semimetals, e.g., Table 1) and does not require the involvement of multiple bands for the charge compensation. The other type of MR comes from charge compensation in the two-band model and it accompanies other transport and magnetic characteristics within the conventional framework.

Using a combination of magnetic susceptibility and magnetotransport measurements to interrogate the different facets of magnetoresistance, we are able to categorize the phosphides into the former and the antimonates into the latter. Our results can be summarized as follows and are depicted in Fig. 1: (i) In the phosphides, the magnitude of $\tan\theta_H$ saturates to an H -independent constant at low temperatures when $H > H_S \simeq 8 \text{ T}$, while $\rho_{xx}(T)$ has a peculiar H -dependent nonmonotonic form. The measured MR defined as $\Delta\rho/\rho_0 \propto H^\alpha$ at low T exhibits a crossover from quasi-linear ($\alpha \sim 1.5 \pm 0.1$) to linear ($\alpha \sim 1.0 \pm 0.1$), where the crossover field, H_S is set by the scale at which $\tan\theta_H(H)$ saturates. In $H > H_S$, MR remains linear in H up to $\mu_0 H = 31 \text{ T}$, the highest applied field in this study. Finally, $\chi(T)$ s for the phosphides exhibit a pronounced minimum at T_{\min} . All of these features can be explained if we assume that the phosphides are semimetals with linear dispersion, even without invoking compensation, and that the MR arises due to guiding center motion (see, e.g., ref. 25 for a recent discussion). Moreover, $\chi(T)$ allows us to extract doping levels relative to the charge neutrality point as fit parameters. (ii) Meanwhile, in the antimonates, the Hall angle remains close to zero ($< 10^{-2}$) at all accessible fields in this study. The MR is nearly quadratic in H from room temperature down to $T = 0.3 \text{ K}$, obeying Kohler's rule. The field dependence of the Hall resistivity strongly deviates from

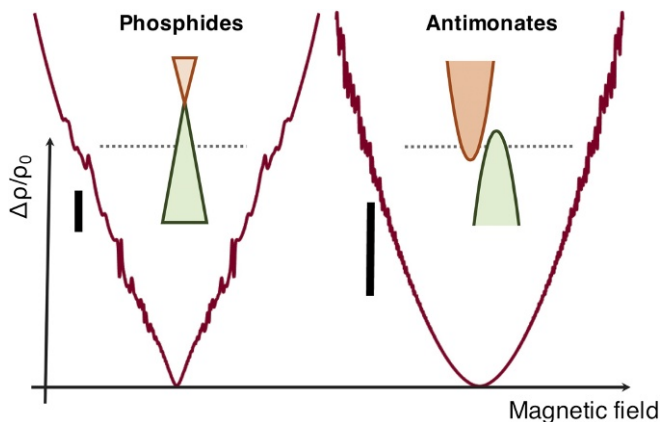


Fig. 1. Schematically depicted nonsaturating MR phenomena and representative energy dispersions for phosphides (TaP) (Left) and antimonates (TaSb₂) (Right). The phosphides' MR is characterized by quasi-linear to linear transition as H increases, while the antimonates' MR is characterized by persistent quadratic H dependence, arising from semiclassical charge compensation. Each bar indicates $\Delta\rho/\rho_0 = 5 \times 10^5\%$. Magnetic field was applied up to $\mu_0 H = 31 \text{ T}$ at $T = 0.3 \text{ K}$.

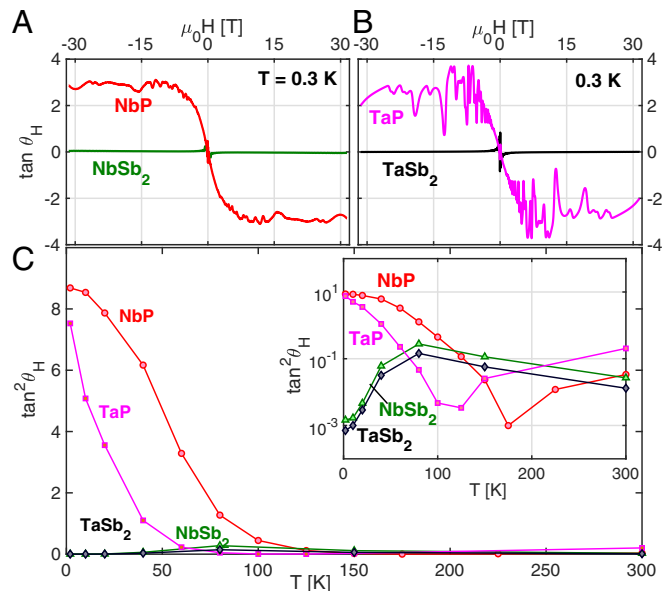


Fig. 2. (A and B) The Hall angle $\tan\theta_H$ (A) for NbP (red) and NbSb₂ (green) as a function of H and (B) for TaP (magenta) and TaSb₂ (black), measured at $T = 0.3 \text{ K}$. Strong quantum oscillations in phosphides result in spike-like features. (C) $\tan^2\theta_H$ measured at $\mu_0 H = 7 \text{ T}$ as a function of T . (Inset) $\tan^2\theta_H$ vs. T plotted in log-scale in the y axis scale, where NbSb₂ and TaSb₂ data are clearly resolved.

linearity in the antimonates. The diamagnetic susceptibility for the antimonates is mostly T independent. These features of the antimonates are archetypical for compensated semimetals with the usual quadratic bands.

Our finding is well consistent with existing electronic structure calculations: NbP and TaP have been studied thoroughly via first-principle calculations and photoemission studies (17, 27, 28), where multiple Weyl nodes were identified in the vicinity of the Fermi energy. The calculations for NbSb₂ and TaSb₂ are also consistent with our picture of nearly compensated semimetals (29), yet the photoemission studies are not yet available for the antimonates.

Single crystals of NbP, TaP, NbSb₂, and TaSb₂ were grown using the chemical vapor transport method following a known synthesis procedure (17, 30–32). Standard electrical contacts were made directly on single crystals, using Ag paint (Dupont 4966) with contact resistance ranges of $\leq 1-2 \Omega$. The magnetotransport measurements were performed with the applied field perpendicular to the direction of current on the plane up to 31 T down to 0.3 K. Magnetic susceptibilities of the samples were measured by the Magnetic Properties Measurements System by Quantum Design.

Results

Magnetotransport. Fig. 2A and B displays $\tan\theta_H$ as a function of H at $T = 0.3 \text{ K}$. In the high-field limit, the phosphides and the antimonates show sharply contrasting behavior: $\tan\theta_H$ for NbP and TaP reaches large values saturating to around 2.5 when $H > H_S \simeq 8 \text{ T}$, while it remains two orders of magnitude smaller for the antimonates (except near zero field). Strong Schubnikov–de Haas oscillations are apparent in both ρ_{xx} and ρ_{xy} that generate spike-like features in the phosphides. In the antimonates, quantum oscillations emerge as well, but only in higher fields and the magnitudes are much smaller due to the smaller Fermi surfaces of the antimonates (29, 33, 34).

The phosphides and antimonates also display contrasting T dependence in Hall angle. Fig. 2C shows the temperature

dependence of $\tan^2 \theta_H$ measured at $\mu_0 H = 7$ T. Strikingly, $\tan^2 \theta_H$ rises rapidly above unity with decreasing T around 100 K and 60 K, for NbP and TaP, respectively. In contrast, the antimonates behave in the opposite fashion: Upon decreasing temperature, $\tan \theta_H$ rapidly decreases, giving values two orders of magnitude smaller than the phosphides (Fig. 2C, *Inset*). We note that small Hall angles are frequently found in conventional metals and semimetals (35), as well as in a wide range of XMR materials with high mobilities for both holes and electrons (19, 22).

The field dependence of $\tan \theta_H$ plays a deciding role in determining MR. For example, a field-independent $\tan \theta_H$ indicates the field dependence of ρ_{xx} and ρ_{xy} should have the same functional form. In uncompensated systems, ρ_{xy} has an H -linear Hall contribution (i.e., $\rho_{xy} = \mu_0 R_H H$, where R_H is the normal Hall coefficient), allowing a field-independent $\tan \theta_H$ and therefore a nonsaturating H -linear ρ_{xx} . This is exactly what we observe in the phosphides which exhibit H -linear ρ_{xy} as well as H -linear ρ_{xx} (below).

Furthermore, large $\tan \theta_H$ can act to suppress resistivity and morph its T dependence. To demonstrate this, we express ρ_{xx} in terms of $\tan \theta_H$ and σ_{xx} ,

$$\rho_{xx} = \frac{\sigma_{xx}}{\sigma_{xx}^2 + \sigma_{xy}^2} = \rho'_{xx} \left(\frac{1}{1 + \tan^2 \theta_H} \right), \quad [1]$$

where $\rho'_{xx} \equiv \frac{1}{\sigma_{xx}}$. As evident in Eq. 1, when $\tan \theta_H \geq 1$, the inverse relation between σ_{xx} and ρ_{xx} no longer holds.

The effect of large $\tan \theta_H$ magnitude on $\rho_{xx}(T)$ is particularly pronounced for NbP and TaP in Fig. 3A and B, where the T dependence of ρ_{xx} is plotted. Monotonic metallic T dependence switches to nonmonotonic behavior as the field increases, with a peak at a temperature that coincides with the onset of rapid increase of $\tan \theta_H$ (Fig. 1C). Crucially, ρ'_{xx} (as defined in Eq. 1) plotted as dashed lines in Fig. 3A and B, *Insets*, deviates significantly from the measured ρ_{xx} , reflecting the large values of $\tan \theta_H$ and the dominant role $\tan \theta_H$ has in $\rho_{xx}(T)$.

NbSb₂ and TaSb₂, however, display contrasting behavior plotted in Fig. 3C and D. We first note that $\rho_{xx}(T)$ initially exhibits a slight decrease in ρ_{xx} as T is lowered until the sudden rise, mimicking a metal-insulator-like transition. This behavior is commonly observed in many XMR materials and ρ_{xx} continues increasing as T is lowered further. In contrast to phosphides in Fig. 3A and B, NbSb₂ and TaSb₂, however, display $\rho_{xx} \approx 1/\sigma_{xx}$ as reflected by the near overlay of the dashed lines and solid lines

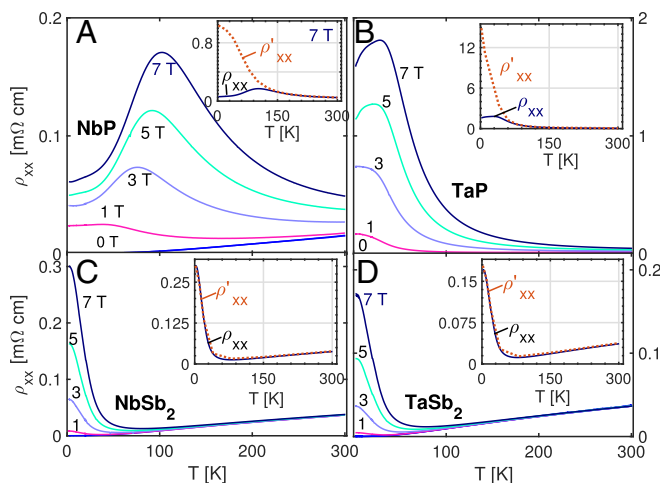


Fig. 3. $\rho_{xx}(T)$ at different H s is shown for (A) NbP, (B) TaP, (C) NbSb₂, and (D) TaSb₂. $\rho'_{xx}(T)$ at $\mu_0 H = 7$ T, defined in Eq. 1, is plotted in A–D, *Insets*.

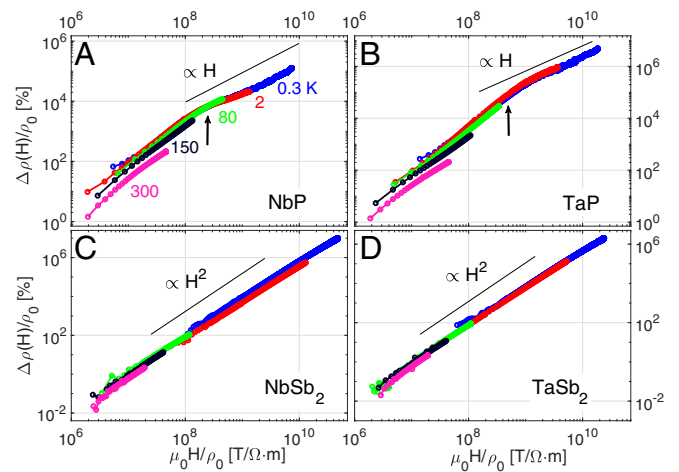


Fig. 4. (A–D) Kohler's plots of phosphides in (A) NbP and (B) TaP and of antimonates in (C) NbSb₂ and (D) TaSb₂. Arrows in A and B indicate the locations of H_S , where $\tan \theta_H$ saturates and the MR switches to H linear.

in Fig. 3C and D, *Inset*. This is consistent with a small $\tan \theta_H \ll 1$. For all samples, the rapid rise in ρ'_{xx} at low temperatures corresponds to a plummeting σ_{xx} .

We now turn to the field dependence of MR. We show Kohler's plots in Fig. 4 and find that $\Delta\rho/\rho_0 \propto H^\alpha$, where $\rho_0 = \rho_{xx}(T, H=0)$, collapses into a single curve over the large T range. In the antimonates, we observe $\alpha \approx 2$ in the entire temperature range up to 31 T. In contrast, in the phosphides the exponent α deviates from 2 even at low H ($\alpha \approx 1.4 \pm 0.1$) and switches over to the linear- H dependence ($\alpha \approx 1$) in the $\mu_0 H \geq 8$ T, where the $\tan \theta_H$ approaches a constant value.

Finally, $\rho_{xy}(H)$'s of NbP and NbSb₂ are compared in Fig. 5A and B. The field dependence of NbSb₂, shown in Fig. 5B, is far from linear and a higher power of H becomes more visible with increasing H . ρ_{xy} in TaP and TaSb₂ showed similar behavior as presented in *SI Appendix*, Fig. S2.

Magnetic Susceptibility. In Fig. 6, we plot the T dependence of the magnetic susceptibility in the low-field limit. All four samples show negative susceptibilities, corresponding to diamagnetism. Fig. 6 displays χ as a function of T for (Fig. 6A) NbP and NbSb₂ and (Fig. 6B) TaP and TaSb₂. Both NbP and TaP have broad yet pronounced minima emerging at $T_{\min} = 203$ K and $T_{\min} = 68$ K, respectively. For TaP the minimum susceptibility (Fig. 6) and the resistivity peak under the field (Fig. 3B) both occur at similar temperatures, which are also close to the temperature where $\tan^2 \theta_H$ first becomes appreciable (Fig. 2C). For NbP, these temperatures are within a factor of 2, although the agreement is not as close as for TaP.

On the other hand, $\chi(T)$ for the antimonates remains featureless and mostly constant.

Discussion

We begin by discussing the magnetic susceptibility plots shown in Fig. 6. The absence of Pauli paramagnetism in all samples indicates that we do not have spin degenerate bands and is strong evidence for spin-momentum locking, such that the magnetic susceptibility is dominated by orbital diamagnetism (36). As we now discuss, the additional features can be well explained if we postulate that the phosphides are uncompensated semimetals with a linear dispersion, whereas the antimonates are compensated semimetals.

We discuss first the phosphides. In particular, we fit the $\chi(T)$ s of phosphides to the result of orbital magnetism in a linear

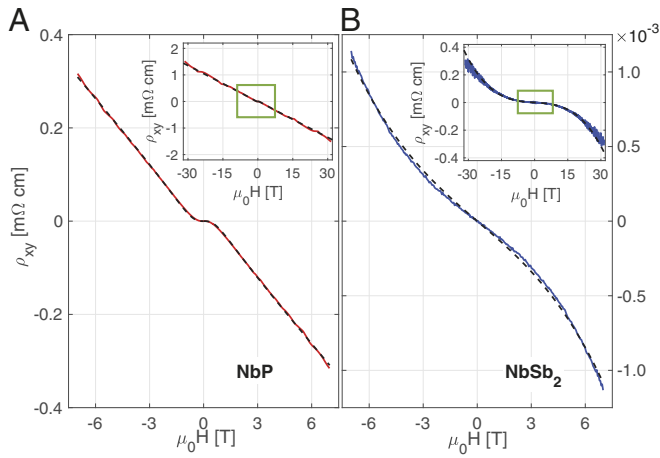


Fig. 5. $\rho_{xy}(H)$ as a function of H in (A) NbP and (B) NbSb₂, measured at $T = 0.3$ K. Note the difference of the magnitude of ρ_{xy} . Dashed line in A shows a fit to Eq. 3 and dashed line in B shows a fit to a two-band model (SI Appendix, section 1). $\rho_{xy}(H)$'s up to 31 T are shown in A and B, Insets, where the small boxes correspond to the main panels.

dispersion (37), which is obtained from energy minimization for the case of a simple linear band crossing (SI Appendix, section 5C)

$$\chi(T) = C \int_0^{\epsilon_0} \frac{\eta(\mu_i/k_B T) - \eta(-\mu_i/k_B T)}{\epsilon} d\epsilon, \quad [2]$$

where η is the standard Fermi–Dirac distribution function, ϵ_0 is a cutoff energy, μ is the chemical potential measured from E_F to the charge neutrality points, and C is a constant in the order of unity. The data for NbP and TaP are well fitted (Fig. 6) by Eq. 2. For NbP, we find one linear crossing point with $\mu = -40$ meV, which is consistent with one of the reported locations of Weyl points in NbP (-57 meV and $+5$ meV) (34). For TaP, we find two crossing points, $\mu_1 = -51$ meV and $\mu_2 = +11$ meV. This is again remarkably consistent with the location of a pair of Weyl nodes reported in photoemission data at -40 meV and $+20$ meV (28). The magnetic susceptibility data thus strongly suggest that the phosphides should be understood as uncompensated semimetals with linear dispersion.

This basic conjecture is also consistent with all our observed transport data on the phosphides. In particular, we note that in the presence of smooth disorder, guiding centers can diffuse in an unusual way to naturally lead to an H -linear ρ_{xx} (24, 25). This arises when the cyclotron radius is smaller than the disorder correlation length (at large enough fields), enabling the guiding center trajectories to become squeezed along the field direction, and exhibits a σ_{xx} that has a dominant $1/H$ dependence (25). We note that this scenario (which is operative only for uncompensated semimetals with smooth disorder) also gives an H -linear ρ_{xy} . Indeed, writing ρ_{xy} in terms of σ_{xx} and σ_{xy} (25), we obtain

$$\rho_{xy} = \frac{\sigma_{xy}}{\sigma_{xy}^2 + \sigma_{xx}^2} = \frac{ne/H}{(ne/H)^2 + (b_0/H + \tilde{b}/H^2)^2}, \quad [3]$$

where b_0 and \tilde{b} are system-specific parameters (25). In the large-field limit, this yields H -linear ρ_{xy} , while in the low-field limit a cubic H dependence arises. The dashed line in Fig. 5A is a fit to Eq. 3 and finds good agreement between data and this analytic form, with $n_e = 1.9 \times 10^6$ C/m³, $b_0 = 5.6 \times 10^5$ C/m³, and $\tilde{b} = 1.5 \times 10^6$ C·T/m³. Additionally, these parameters confirm that $1/H$ -like dependence dominates σ_{xx} for fields larger than several teslas, as we find clearly in our data.

Central to linear MR is a field-independent $\tan \theta_H$, consistent with observations on the phosphides at fields above $H_S \simeq 8$ T (Fig. 2). Specifically, when the cyclotron radius is smaller than the disorder correlation length, ref. 25 estimates a $\tan \theta_H$ as

$$\tan \theta_H \approx \frac{2}{\sqrt{27}\pi} \left(\frac{\mu}{eV_0} \right)^{3/2}, \quad [4]$$

where μ is the chemical potential and V_0 is the disorder strength (typical fluctuation in local chemical potential). Taking the values for μ from the magnetic susceptibility fit (for TaP taking the larger of the μ values, since the valley with larger Fermi surface will provide most of the carriers), we obtain $V_0 \approx 7$ mV for NbP and $V_0 \approx 10$ mV for TaP.

We note that linear MR is expected to disappear for $k_B T \gg V_0$ (25) when inelastic scattering degrades the squeezed trajectories of guiding centers. These are expected to occur above a temperature scale or order of $\frac{V_0}{k_B} \approx 90$ K and 120 K for NbP and TaP, respectively. In NbP the estimated T scales are consistent with the T scale on which nonmonotonicity is observed in Fig. 3A and with the temperature dependence of the Kohler plots in Fig. 4A. In fact, these two T scales also correspond to where $\tan \theta_H(T)$ measured at H_S begins to rise rapidly (Fig. 1C). In TaP, the observed temperature scale is around 60 K (instead of the expected 120 K); however, we remind the reader that it is hard to cleanly separate out the V_0 scale from MR, because other thermally activated scatterings become important at elevated temperature.

We can also extract the disorder correlation length (ξ) from the condition that the cyclotron radius (r_C) is of the same order as the disorder correlation length at $H_S \approx 8$ T, above which $\tan \theta_H$ becomes field independent. At $H = H_S$, the ξ is on the order of $r_C = \frac{mv_F}{eB}$ and it is estimated to be 26 nm and 14 nm for NbP and TaP, respectively, using Fermi velocities (v_F 's) from the reported values (17, 27, 33). It is interesting to note that the values of ξ are consistent with the length scales for defects and stacking faults that were revealed in TaP (38).

Meanwhile, a field-independent $\tan \theta_H$ and an H -linear ρ_{xy} automatically imply an H -linear MR at high fields, consistent with Fig. 4. Finally, the temperature dependence of ρ_{xx} (Fig. 3) can also be understood within this framework. The key point to note is that these systems have linear dispersion with small doping, such that the density of states at the Fermi level is small,

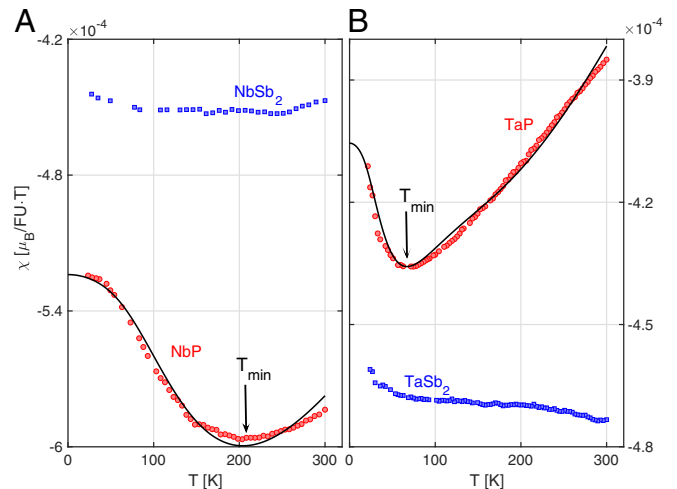


Fig. 6. (A and B) χ vs. T in the phosphides (red) and antimonates (blue), measured at $\mu_0 H = 1$ T. Solid line is fit to Eq. 2, which gives $\mu = -40$ meV for one linear node for NbP (A) and $\mu_1 = 51$ meV and $\mu_2 = -11$ meV for two linear nodes for TaP (B). Arrows indicate the locations of T_{\min} (main text).

$\sim \mu^2$. Increasing the temperature T allows the system to access states within $k_B T$ of the chemical potential and (since the density of states grows rapidly with energy), greatly enhances the number of states that can participate in transport. We thus conclude that increasing temperature can increase σ_{xx} through this density of states effect, consistent with the observed monotonic decline in ρ'_{xx} with increasing temperature (Fig. 3A–D, Insets).

These, together, establish that all salient observed features of the phosphides can be explained by an uncompensated spin–orbit locked semimetal with linear dispersion; this is corroborated by our linear MR-type magnetotransport expected from guiding center diffusion that is particularly pronounced in semimetals with linear dispersion (25). Moreover, a systematic combination of thermodynamic and magnetotransport measurements can allow us to extract parameters such as chemical potential (or doping level) and typical disorder strength and correlation length. These enable us to make a direct correspondence with a microscopic guiding center description, e.g., identification of fields above which linear MR dominates and identification of temperature scales below which $\tan \theta_H$ becomes large and H independent.

The antimonates also exhibit diamagnetism, indicating that these materials are also spin–orbit coupled, but their magnetic susceptibility is not well fitted by an expression of the type of Eq. 2. Instead, the susceptibility is mostly temperature independent, closer to the expectation for Landau diamagnetism for quadratic bands (36). These materials also exhibit a MR that is $\sim H^2$. These facts, as well as the smallness of $\tan \theta_H$ in the antimonates, are all well explained if we postulate that these systems are compensated semimetals described by a two-band model (SI Appendix, section 1). In compensated semimetals, $\tan \theta_H$ is small, as long as mobilities of carriers remain in a similar range, and the MR is $\sim H^2$, consistent with observation. The MR is nonsaturating for perfect compensation, but will eventually saturate at a value $\sim 1/\delta n^2$, where δn is the difference between electron and hole densities. We ascribe the lack of saturation of MR up to 31 T to the systems being close enough to compensation that we do not hit the saturation value at experimentally accessible fields. Here we note that, despite high mobilities of both carriers in antimonates (SI Appendix, Table S1) that satisfy the condition of $\nu B \gg 1$, $\tan \theta_H$ is found to be much less than unity. This implies that the system effectively remains in the limit of $\omega_c \tau \ll 1$ and the MRs of the antimonates should not be saturated within the experimentally accessible field range of this work.

The field dependence of ρ_{xy} is also informative. With small deviation from perfect compensation, one expects (SI Appendix, section 4) that $\rho_{xy} \sim H$ for systems with linear dispersion, but for quadratic dispersion one expects $\rho_{xy} \sim H$ at low fields, with a crossover to $\rho_{xy} \sim H^3$ at higher fields. The data in Fig. 5 are more consistent with the latter behavior, suggesting that the NbSb₂ should be thought of as compensated semimetals with effectively quadratic dispersion (i.e., appreciable band curvature on the scale of the doping level). This conclusion is also consistent with the magnetic susceptibility data, which are reminiscent of the Landau diamagnetism of quadratic bands.

Summary

We investigated magnetotransport and magnetic susceptibility of four different semimetals. We find that the combination of susceptibility and magnetotransport measurements allows us to cleanly characterize the nonsaturating behavior of MR. The two phosphide materials that we study (NbP and TaP) are well described by a model of uncompensated semimetals with linear dispersion, wherein the MR is well described by guiding center diffusion with $\tan \theta_H \gg 1$ and field independent. The combination of measurements that we have made also allows us to extract the disorder strength and disorder correlation length in these materials, as well as the doping level. Meanwhile, the antimonates (NbSb₂ and TaSb₂) are well described as compensated semimetals governed by a two-band model with effectively quadratic bands and $\tan \theta_H \ll 1$. The criteria reported here highlight a distinct set of traits for nonsaturating MR and will serve as a primary touchstone to classify MR phenomena in materials, which in turn will provide design principles for material platforms and devices for technological application.

ACKNOWLEDGMENTS. We thank David Graf for technical assistance with the high-field measurement. This work was supported by the University of Colorado Boulder Office of Research Innovation. High-magnetic-field data were obtained at the National High Magnetic Field Laboratory, which is supported by National Science Foundation Cooperative Agreement DMR-1157490 and the State of Florida. This research was sponsored in part by the Army Research Office and was accomplished under Grant W911NF-17-1-0482 (to Y.-P.L. and R.M.N.). J.C.W.S. acknowledges the support of the Singapore National Research Foundation (NRF) under NRF Fellowship Award NRF-NRFF2016-05. The views and conclusions contained in this document are those of the authors and should not be interpreted as representing the official policies, either expressed or implied, of the Army Research Office or the US Government. The US Government is authorized to reproduce and distribute reprints for Government purposes notwithstanding any copyright notation herein.

- Ashcroft NW, Mermin ND (1976) *Solid State Physics* (Brooks/Cole, Harcourt College Publishers, Fort Worth, TX).
- Xu R, et al. (1997) Large magnetoresistance in non-magnetic silver chalcogenides. *Nature* 390:57–60.
- Yang FY, et al. (1999) Large magnetoresistance of electrodeposited single-crystal bismuth thin films. *Science* 284:1335–1337.
- Lee M, Rosenbaum TF, Saboungi ML, Schnyder HS (2002) Band-gap tuning and linear magnetoresistance in the silver chalcogenides. *Phys Rev Lett* 88:066602.
- Husmann A, et al. (2002) Megagauss sensors. *Nature* 417:421–424.
- Parish MM, Littlewood PB (2005) Classical magnetotransport of inhomogeneous conductors. *Phys Rev B* 72:094417.
- Kisslinger F, Ott C, Weber HB (2017) Origin of nonsaturating linear magnetoresistivity. *Phys Rev B* 95:024204.
- Abrikosov AA (1998) Quantum magnetoresistance. *Phys Rev B* 58:2788–2794.
- Solin SA, et al. (2002) Nonmagnetic semiconductors as read-head sensors for ultra-high-density magnetic recording. *Appl Phys Lett* 80:4012–4014.
- Branford WR, et al. (2005) Geometric manipulation of the high-field linear magnetoresistance in InSb epilayers on GaAs (001). *Appl Phys Lett* 86:202116.
- Hu J, Rosenbaum TF (2008) Classical and quantum routes to linear magnetoresistance. *Nat Mater* 7:697–700.
- Narayanan A, et al. (2015) Linear magnetoresistance caused by mobility fluctuations in n -doped Cd_3As_2 . *Phys Rev Lett* 114:117201.
- Liang T, et al. (2015) Ultrahigh mobility and giant magnetoresistance in the Dirac semimetal Cd_3As_2 . *Nat Mater* 14:280–284.
- Luo Y, et al. (2016) Anomalous electronic structure and magnetoresistance in TaAs_2 . *Sci Rep* 92:27294.
- Huang X, et al. (2015) Observation of the chiral-anomaly-induced negative magnetoresistance in 3D Weyl semimetal TaAs. *Phys Rev X* 5:031023.
- Lv BQ, et al. (2015) Experimental discovery of Weyl semimetal TaAs. *Phys Rev X* 5:031013.
- Shekhar C, et al. (2015) Extremely large magnetoresistance and ultrahigh mobility in the topological Weyl semimetal candidate NbP. *Nat Phys* 11:645–649.
- He J, et al. (2016) Distinct electronic structure for the extreme magnetoresistance in Ysb. *Phys Rev Lett* 117:267201.
- Ali MN, et al. (2014) Large, non-saturating magnetoresistance in WTe_2 . *Nature* 514:205–208.
- Luo Y, et al. (2015) Hall effect in the extremely large magnetoresistance semimetal WTe_2 . *Appl Phys Lett* 107:182411.
- Zeng LK, et al. (2016) Compensated semimetal LaSb with unsaturated magnetoresistance. *Phys Rev Lett* 117:127204.
- Xu J, et al. (2017) Origin of the extremely large magnetoresistance in the semimetal Ysb. *Phys Rev B* 96:075159.
- Yuan Z, Lu H, Liu Y, Wang J, Jia S (2016) Large magnetoresistance in compensated semimetals TaAs_2 and NbAs_2 . *Phys Rev B* 93:184405.
- Polyakov D (1986) Change, due to scattering-act correlation of electron diffusion in a classically strong magnetic field. *Sov Phys JETP* 63:317.
- Song JCW, Refael G, Lee PA (2015) Linear magnetoresistance in metals: Guiding center diffusion in a smooth random potential. *Phys Rev B* 92:180204.
- Klier J, Gornyi IV, Mirlin AD (2015) Transversal magnetoresistance in Weyl semimetals. *Phys Rev B* 92:205113.
- Lee CC, et al. (2015) Fermi surface interconnectivity and topology in Weyl fermion semimetals TaAs, TaP, NbAs, and NbP. *Phys Rev B* 92:235104.

28. Xu SY, et al. (2015) Experimental discovery of a topological Weyl semimetal state in TaP. *Sci Adv* 1:e1501092.
29. Xu C, et al. (2016) Electronic structures of transition metal dipnictides xpn_2 ($x = \text{Ta}, \text{Nb}; pn = \text{P}, \text{As}, \text{Sb}$). *Phys Rev B* 93:195106.
30. Wang K, Graf D, Li L, Wang L, Petrovic C (2014) Anisotropic giant magnetoresistance in nbsb_2 . *Sci Rep* 4:7328.
31. Li Y, et al. (2016) Resistivity plateau and negative magnetoresistance in the topological semimetal tasb_2 . *Phys Rev B* 94:121115.
32. Zhang CL, et al. (2017) Magnetic-tunnelling-induced Weyl node annihilation in TaP. *Nat Phys* 13:979–986.
33. Arnold F, et al. (2016) Negative magnetoresistance without well-defined chirality in the Weyl semimetal TaP. *Nat Commun* 7:11615.
34. Klotz J, et al. (2016) Quantum oscillations and the Fermi surface topology of the Weyl semimetal NbP. *Phys Rev B* 93:121105.
35. Hurd CM (1972) *The Hall Effect in Metals and Alloys* (Plenum, New York).
36. Blundell S (2001) *Magnetism in Condensed Matter* (Oxford Univ Press, Oxford).
37. Mikitik GP, Sharlai YV (2016) Magnetic susceptibility of topological nodal semimetals. *Phys Rev B* 94:195123.
38. Besara T, et al. (2016) Coexistence of Weyl physics and planar defects in the semimetals TaP and TaAs. *Phys Rev B* 93:245152.